An experimental and numerical study of alkali-activated fly ash paste from dissolution kinetics to microstructure formation

Chen, Yun; Chen, Jiayi; Gupta, Mayank; Liang, Xuhui; de Lima, Luiz Miranda; Xu, Zhiyuan; Zuo, Yibing; Yin, Suhong; Yu, Qijun; Ye, Guang

DOI
10.1016/j.cemconres.2025.107999

Publication date
2025

Document Version
Final published version

Published in
Cement and Concrete Research

Citation (APA)
Chen, Y., Chen, J., Gupta, M., Liang, X., de Lima, L. M., Xu, Z., Zuo, Y., Yin, S., Yu, Q., & Ye, G. (2025). An experimental and numerical study of alkali-activated fly ash paste: from dissolution kinetics to microstructure formation. *Cement and Concrete Research*, *198*, Article 107999. https://doi.org/10.1016/j.cemconres.2025.107999

Cement and Concrete Research 198 (2025) 107999

Contents lists available at ScienceDirect

Cement and Concrete Research

journal homepage: www.elsevier.com/locate/cemconres

An experimental and numerical study of alkali-activated fly ash paste – from dissolution kinetics to microstructure formation

Yun Chen [a,b], Jiayi Chen [a], Mayank Gupta [a], Xuhui Liang [a], Luiz Miranda de Lima [a], Zhiyuan Xu [a], Yibing Zuo [c], Suhong Yin [b], Qijun Yu [b], Guang Ye [a,*]

[a] Section of Materials and Environment, Faculty of Civil Engineering and Geosciences, Delft University of Technology, Delft 2628CN, the Netherlands
[b] School of Materials Science and Engineering, South China University of Technology, Guangzhou 510640, Guangdong, China
[c] School of Civil and Hydraulic Engineering, Huazhong University of Science and Technology, Wuhan 430074, China

ARTICLE INFO

Keywords:
Alkali-activated fly ash
Dissolution kinetics
N-(C-)A-S-H gels
3D microstructure evolution
GeoMicro3D model

ABSTRACT

This study presents an extended numerical approach based on GeoMicro3D to simulate the reaction kinetics and three-dimensional (3D) microstructure evolution of alkali-activated fly ash (AAFA). Dissolution experiments were conducted under varying NaOH concentrations and temperatures to formulate predictive rate functions for Si and Al release. These experimentally derived kinetic functions, alongside a thermodynamic dataset for N-(C-)A-S-H gels, were incorporated into the GeoMicro3D model to capture the chemical reactions and 3D microstructure evolution of AAFA. The model well captured reaction degree of fly ash, formation of solid products, evolution of pore solution compositions, and porosity over time. Notably, it is the first to predict the time-dependent spatial distribution of phases within the 3D AAFA microstructure by integrating kinetic and microstructural modeling. Dual validation using both dissolution data and microstructural metrics demonstrates the model's reliability and robustness. This integrated framework provides new insights into the coupled chemical–microstructural evolution of alkali-activated materials.

1. Introduction

Driven by the demand for environmental protection, alkali-activated fly ash (AAFA) has stood out as a sustainable, cement-free binder, known for its low carbon emissions and favorable engineering properties when properly formulated [1,2]. Despite its potential, AAFA's broader adoption has been restricted by the variability and unpredictability of its engineering properties, which are directly linked to its diverse microstructures. These microstructures are influenced by various factors, including the intrinsic characteristics of the fly ash, the composition of mixtures, and the curing conditions, all of which have been extensively explored through experimental studies [3–5]. However, a significant challenge in predicting the microstructure-related engineering properties of AAFA lies in the absence of numerical models to simulate its microstructure.

The microstructure of AAFA evolves through a series of reactions involving the dissolution of fly ash particles and the formation of reaction products. Accurate modeling of the microstructural development, therefore, requires simulating these underlying chemical reactions. Thermodynamic modeling is theoretically robust for simulating the chemical equilibria of these reactions. However, the application of thermodynamic modeling to AAFA has historically been limited, primarily due to the lack of an appropriate thermodynamic dataset for N-(C-)A-S-H gel, the principal reaction product of AAFA. Our recent work addressed this gap by developing a comprehensive thermodynamic dataset for N-(C-)A-S-H gel [6,7]. Based on that dataset, we successfully applied thermodynamic modeling to simulate the chemical reactions of AAFA [6]. Nevertheless, because the dissolution kinetics of fly ash were not yet fully understood, thermodynamic modeling of AAFA to date has assumed the congruent dissolution of various oxides in fly ash.

While thermodynamic modeling captures the final equilibrium state of the system, accurately predicting the time-dependent development of AAFA microstructure also requires a kinetic perspective. In particular, the rate and extent of fly ash dissolution govern the availability of ions for subsequent gel formation. Thus, understanding and modeling the dissolution kinetics of fly ash is a critical complement to AAFA microstructure modeling. Existing research indicates that the dissolution kinetics of fly ash depend on various factors, including the reactivity of fly

* Corresponding author.
E-mail address: G.Ye@tudelft.nl (G. Ye).

https://doi.org/10.1016/j.cemconres.2025.107999
Received 24 February 2025; Received in revised form 20 June 2025; Accepted 10 July 2025
Available online 22 July 2025

ash [8,9], the pH of the solution [10–12] and the temperature [10,11]. However precise mathematical models that quantitatively capture the interplay of these effects remain scarce. A potential approach lies in adapting general silicate glass dissolution models to fly ash. According to the transition state theory, the dissolution rate (r) of silicate glasses from far-from-equilibrium state to near-to-equilibrium states can be described via the following equation:

$$r = r_+\left(1 - \frac{IAP}{K_{sp}}\right) \tag{1}$$

where r_+ is the forward dissolution rate, which refers to the dissolution rate of glass at the far-from-equilibrium condition [13,14]. *IAP* is the ion activity product. K_{sp} is the solubility product of the oxides.

The forward dissolution rate r_+ in Eq. (1), also known as the maximum dissolution rate, refers to the dissolution rate of glass at the far-from-equilibrium condition [13,14]. It is commonly expressed by the Eq. (2) [15–17]:

$$r_+ = k_0 10^{\pm\eta \bullet pH} \exp\left(\frac{-E_a}{RT}\right) \tag{2}$$

where k_0 is the intrinsic rate constant, which was found to be a glass-related parameter [16], η is the pH power law coefficient, E_a is the apparent activation energy.

While this equation accounts for the primary factors influencing fly ash dissolution, the specific parameters required for accurate modeling have yet to be fully established.

Beyond purely chemical reaction modeling, the prediction of AAFA's microstructure has yet to be fully addressed. A promising approach for bridging this gap is the GeoMicro3D model [18], originally developed to simulate both the chemical reaction and three-dimensional (3D) microstructure evolution of alkali-activated slag (AAS). Since AAFA and AAS both fall under the category of AAMs, it is logical to explore extending GeoMicro3D model to AAFA systems. In its original forms, GeoMicro3D predicts the reaction degree, phase assemblages and 3D microstructure of AAS using the physicochemical properties of the raw materials as input. The model first maps the initial spatial distribution of slag particles in an alkaline solution, then simulates dissolution of those particles using built-in kinetic functions. Next, ion diffusion is modeled with the lattice Boltzmann method (LBM) [19,20]. Once saturation or oversaturation is reached, the model employs thermodynamic calculations to predict the formation of reaction products. Adapting this algorithm to AAFA requires two essential inputs: a robust description of fly ash dissolution kinetics and a suitable thermodynamic model for AAFA.

Therefore, the aim of this research is to simulate both the dissolution of fly ash and the 3D microstructural evolution of AAFA. To achieve this, we first experimentally investigate the dissolution of fly ash in NaOH solutions at various temperatures to determine the dissolution kinetics. Based on these results, we establish a prediction function for the fly ash dissolution rate and incorporate it into GeoMicro3D. We then validate this function by comparing simulation results to experimental data. Subsequently, we integrate the thermodynamic dataset for N-(C-)A-S-H gel, as developed in [6,7], into GeoMicro3D to provide a basis for the thermodynamic modeling of AAFA. The extended GeoMicro3D model is then employed to simulate the reaction process and 3D microstructural evolution of AAFA. We analyze the simulated results in terms of 3D microstructure, phase assemblage evolution, degree of reaction of fly ash, pore solution chemistry, and porosity. Experimental results on AAFA pastes, obtained both in this study and [6], are presented for comparison, thereby validating the extended GeoMicro3D model. The developed model for AAFA microstructure establishes a foundation for further multiscale modeling approaches to predict mechanical properties and long-term durability. By linking microstructural features to macroscopic performance, this modeling tool can assist in the mix design for targeted performance and improved sustainability, thereby supporting the broader adoption of AAFA in real-world construction applications [21–23].

2. Materials and experimental methods

2.1. Materials

In this study, fly ash was used to investigate its dissolution rate in alkaline solutions and to prepare AAFA paste. The chemical composition of fly ash, determined by X-ray fluorescence spectroscopy (XRF), is listed in Table 1. According to the definition criteria in [24], this fly ash is classified as Class F. The particle size distribution (PSD) of the fly ash, measured by laser diffraction (Fig. 1), reveals a median particle size (d_{50}) of 43.3 μm. The X-ray diffraction (XRD) pattern of the fly ash is shown in Fig. 2. Based on the content of crystalline phases from quantitative X-ray diffraction (QXRD) results, the chemical composition of the amorphous fraction is calculated, as also shown in Table 1.

Sodium hydroxide (NaOH) solutions were prepared by dissolving sodium hydroxide pellets (>98 wt%) in deionized water.

2.2. Dissolution of fly ash

To determine forward dissolution rate of fly ash, the dissolution experiment was performed as follows: 0.1 g of fly ash was mixed with 100 mL of NaOH solution with different concentrations in a sealed container. A high solution-to-ash ratio of 1000 was chosen to prevent the formation of any reaction products. Each mixture was then placed in a temperature-controlled shaker set at 250 rpm with experiments performed at different temperatures as detailed in Table 2. At specific time intervals over a total duration of 48 h, samples were collected by filtering the mixture through a 0.2 μm filter. Separate samples were prepared for each time point rather than sampling repeatedly from the same solution. Filtration was completed within seconds, and the filtrates were immediately sealed in completely filled polypropylene bottles to avoid contact with CO_2. All samples were stored under sealed conditions and analyzed by ICP-OES (inductively coupled plasma optical emission spectroscopy) within 2 days.

The concentration of Si, Al and Ca in the filtrate was measured by a Perkin Elmer Optima 5300 DV ICP-OES system following a dilution step with 0.2 vol% nitric acid. Calibration was performed using multi-element standard solutions covering a range of concentrations (e.g., Si: 0–0.2 mmol/L, Al: 0–0.05 mmol/L, and Ca: 0–0.05 mmol/L). Calibration curves were verified and repeated every 5 samples to account for instrumental drift. The reported concentrations represent the average of three replicate measurements for each condition. Based on the elemental concentrations over time, the forward dissolution rate (mol/m^2/s) of the specific element (X) can be computed with the following equation:

$$r_{+,X} = \frac{\Delta(X)}{\Delta t}\frac{V}{m^* SSA} \tag{3}$$

Table 1
Chemical compositions of fly ash (by wt%).

Oxides	SiO_2	Al_2O_3	Fe_2O_3	CaO	MgO	K_2O	Na_2O	P_2O_5	TiO_2	SO_3	LOI
Total	56.75	24.58	5.76	3.93	2.10	1.40	1.27	1.17	1.03	0.68	1.33
Amorphous	44.41	17.89	5.12	3.63	2.10	1.40	1.27	1.17	1.03	0.68	–

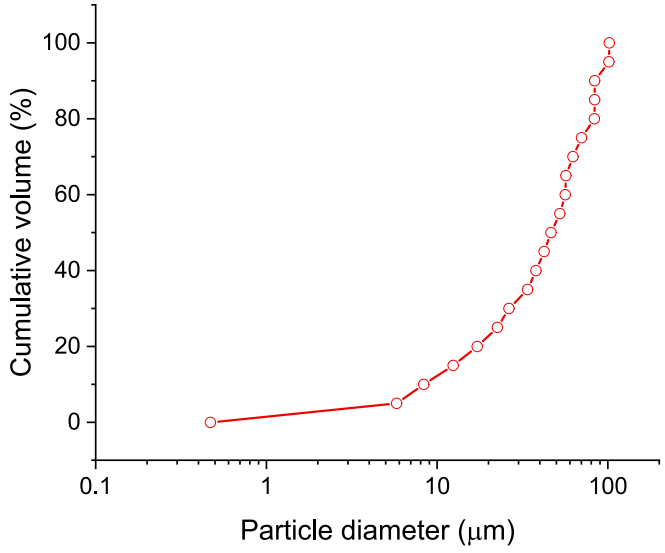

Fig. 1. Particle size distribution of fly ash.

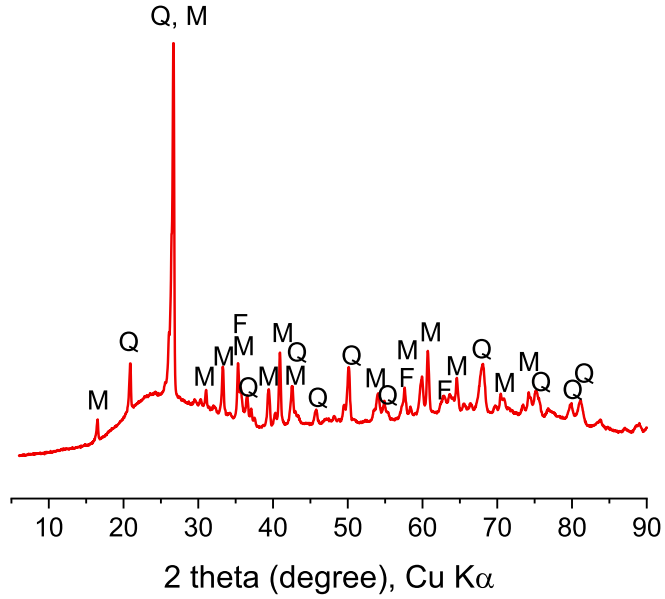

Fig. 2. XRD pattern of fly ash. M: mullite; Q: quartz; F: magnetite.

Table 2
Experimental conditions for the dissolution tests.

Group	NaOH concentration	pH of NaOH solution	Temperature
1	1 M	14.00	20 °C
2	1.5 M	14.18	20 °C
3	3 M	14.48	20 °C
4	5 M	14.70	20 °C
5	5 M	14.70	40 °C
6	5 M	14.70	60 °C

where $\Delta(X)$ denotes the change in elemental concentration (mol/L) over the time increment Δt (s), V is the solution volume (L), m is the mass of fly ash (g), *SSA* represents the specific surface area of fly ash, which was determined as 1.01 m^2/g using the Brunauer-Emmett-Teller (BET) method.

2.3. Mixture and characterization of AAFA paste

AAFA pastes were prepared by mixing fly ash with a NaOH solution containing 9.3 wt% Na_2O (relative to the fly ash mass) at a water-to-ash ratio of 0.35, following the procedure described in [6]. The samples were then cured in sealed containers at 40 °C. After 7 days and 28 days of curing, the samples were cut into small pieces (approximately 1–2 cm^3) and immersed in isopropanol for two weeks to halt further reactions. Subsequently, they were freeze-dried at −24 °C under a vacuum of 10^{-1} Pa.

To access the modeling result, the porosity of AAFA paste was measured using mercury intrusion porosimetry (MIP) on a Micrometrics PoreSizer® 9500 instrument. The MIP measurement began with a low-pressure stage ranging from 0 to 0.14 MPa, followed by a high-pressure stage from 0.14 to 210 MPa. After the intrusion procedure, pressure was decreased from 210 to 0.14 MPa for the extrusion process. A surface tension of 0.485 N/m and a contact angle of 141° were used.

3. Numerical simulation program

3.1. Extended GeoMicro3D model

The extended GeoMicro3D model framework is depicted in Fig. 3, comprising four key components: (i) initial structure simulation, (ii) fly ash dissolution, (iii) ion diffusion, and (iv) nucleation of reaction products with thermodynamic modeling. Since the framework of the extended GeoMicro3D is similar to the original one, which is thoroughly described in [18], the introduction below aims to provide a basic understanding of the algorithm of the model, without covering all detailed aspects. Note that the detailed parameters used in simulations will be provided in Sections 3.2 and 3.3.

(i) initial structure simulation

The initial structure is built using the Anm model [25], which simulates the initial spatial distribution of precursor (fly ash in this case) within an alkaline activator solution. In the Anm model, the fly ash particles are placed into the simulation box sequentially, from large size to small size. The particle shapes are described using their spherical harmonic coefficients derived from digital micro X-ray computed tomography images of real fly ash particles. This approach enables a realistic reconstruction of individual particle geometries, capturing critical morphological features such as angular edges and surface roughness. Further details can be found in [25,26]. Internal voids within fly ash are introduced digitally after parking, based on volume differences derived from measured apparent and real densities as demonstrated in Section 3.2.

(ii) fly ash dissolution

The dissolution of fly ash involves the breakage of chemical bonds (e.g., Si—O, Al—O, Ca—O) in its structural framework. It is reported that the relative dissolution rates of these bonds within multioxide structures are comparable to those in the corresponding single oxides [27]. Based on this, the dissolution of fly ash can be described as the dissolution of its individual constituent oxide [28]. The dissolution of silica, aluminum

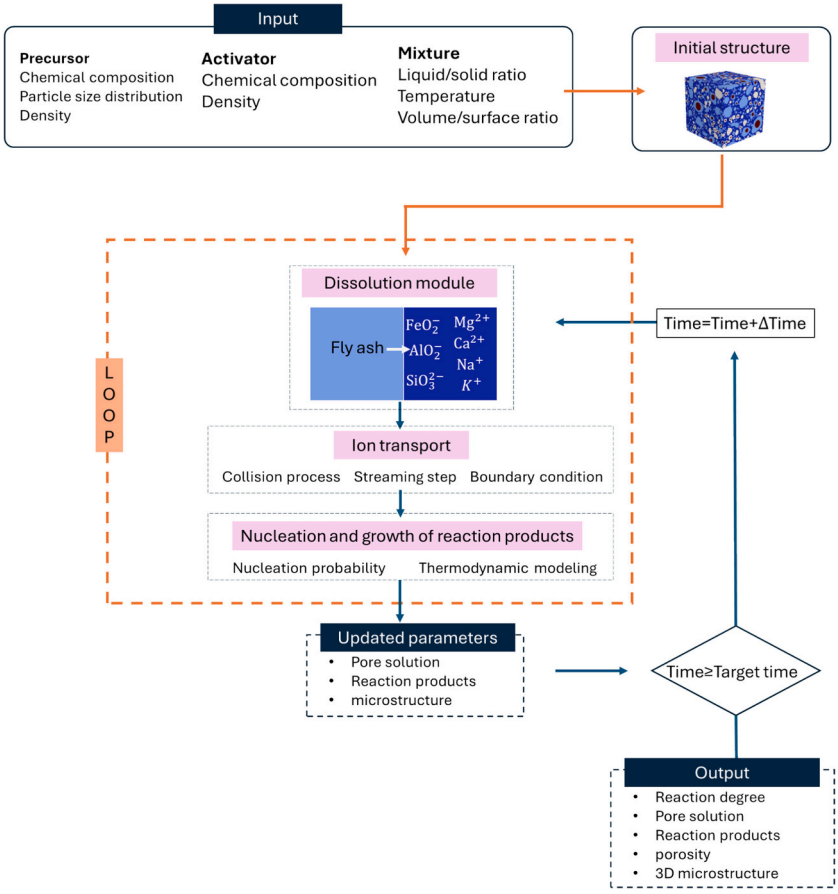

Fig. 3. Framework of extended GeoMicro3D model.

oxide and calcium oxide in an alkaline solution was described as follows:

$$SiO_2 + 2OH^- \rightarrow H_2O + SiO_3^{2-} \tag{4}$$

$$Al_2O_3 + 2OH^- \rightarrow H_2O + 2AlO_2^- \tag{5}$$

$$CaO + H_2O \rightarrow 2OH^- + Ca^{2+} \tag{6}$$

The overall dissolution rates of these oxides are described by Eq. (1, while the forward dissolution rate is determined by the dissolution test as described in Section 2.2. The derivation of function for the forward dissolution rate will be presented in Section 4.2.

As for the minor constituents like Mg, Na, and K, which act as glass modifiers similar to Ca, the dissolution rates of these elements (X) were obtained based on the dissolution rate of Ca:

$$r_X = f_X \frac{v_X}{v_{Ca}} r_{Ca} \tag{7}$$

where v_X and v_{Ca} are the molar fractions of element X and Ca in the fly ash, respectively. f_X is the ratio of the dissolution rate of element X relative to the dissolution rate of Ca.

In contrast, Fe_2O_3 usually functions as a network former in glass, its dissolution rate was established by correlating it with the dissolution rate of Al, using the following equation:

$$r_{Fe} = f_{Fe} \frac{v_{Fe}}{v_{Al}} r_{Al} \tag{8}$$

where v_{Fe} and v_{Al} are the molar fractions of Fe and Al in the fly ash, respectively. f_{Fe} is the ratio of the dissolution rate of Fe relative to the dissolution rate of Al.

Additionally, to mitigate the impact of discrepancies in particle size distribution between the experiment and the model, the following equation is used to align the simulated surface area of the fly ash with the experimentally measured value:

$$r'_{+,X} = \frac{V_{model}/S_{model}}{V_{exp}/S_{exp}} r_{+,X} \tag{9}$$

where $r'_{+,X}$ and $r_{+,X}$ are the forward dissolution rates of element X before and after considering the effect of the solution-volume/surface-area ratio. V_{model} and V_{exp} denote the solution volume in simulation and experiment, respectively, while S_{model} and S_{exp} represent the surface area of the fly ash in simulation and experiment, respectively. The derivation of Eq. 9 can be found in [18,29].

The amounts of dissolved elements from fly ash can be calculated based on the corresponding dissolution rate. Each fly ash voxel has six neighboring cubes, creating six interfaces where dissolution can happen. Similarly, the ions at each voxel come in the solution from the six nearest solid voxels. The amounts of elements dissolved at each interface and at six interfaces can be calculated using Eq. 10 and Eq. (11), respectively.

$$\Delta n_{X,i} = (1 - V_i)^{1.1} r_{X,i} t_0 l_0^2 \tag{10}$$

$$\Delta N_X = \sum_{i=1}^{6} \Delta n_{X,i} \tag{11}$$

where $\Delta n_{X,i}$ and ΔN_X are the dissolved amounts of element X at interface i and six interfaces at one time step t_0, respectively. V_i is the volume fraction of solids in the voxel next to the interface area that is dissolving, $r_{X,i}$ is the dissolution rate of element X at the interface i, l_0 is the side length of a voxel.

(iii) ion diffusion

Following the dissolution step, the diffusion of ions in the microstructure was modeled using the lattice Boltzmann (LB) method [20,30]. A cubic lattice model D3Q7 was employed to simulate the ion transport in the microstructure. The evolution of particle distribution functions satisfies the following lattice Boltzmann equation:

$$f_j(x+e_j\delta t, t+\delta t) = f_j(x,t) - \frac{\delta t}{\tau}\left[f_j(x,t) - f_j^{eq}(x,t)\right] + w_j\delta t S \quad (12)$$

where f_j and f_j^{eq} represent the non-equilibrium and equilibrium particle distribution functions at location x and time t in the direction of the velocity j, respectively. e_j stands for the discrete velocity at location x and time t. w_j is the weighting factor in the velocity direction j (w_j=1/7 for all directions). δt is the LB time step and S signifies the source term, accounting for the amounts of dissolved elements and the amounts of elements consumed during the precipitation of the products at one LB time step. τ denotes the relaxation time. The relationship between the relaxation time τ and the ion diffusivity D_p at any lattice node can be written as:

$$T_0 = L_0^2 e_s^2(\tau - \delta t/2)/D_p \quad (13)$$

where T_0 and L_0 are the time and length factors for conversion between the lattice unit and the real physical unit, respectively. e_s is the lattice speed of sound ($e_s = 0.53$).

f_j^{eq} can be expressed in terms of ion concentration (F) in the lattice node as:

$$f_j^{eq}(x,t) = w_j F(x,t) \quad (14)$$

$$F(x,t) = \sum_{j=0}^{6} f_j(x,t) \quad (15)$$

(iv) nucleation of reaction products with thermodynamic modeling

Following the dissolution of different ions from fly ash, the pore solution may reach a state of saturation or oversaturation. In this state, solid reaction products can form if there are nuclei present or if new nucleation sites are likely to form. Nucleation at any location begins once the nuclei of the reaction product(s) reach a critical size. The probability $P(\Delta t)$ of at least one critical nucleus existing in the solution can be calculated using Eq. (16 [31]:

$$P(\Delta t) = 1 - \exp(-JV\Delta t) \quad (16)$$

where V is the solution volume within which the nucleus forms, Δt is the time interval, while J is the nucleation rate that can be determined using the following equation:

$$J(S) = AS_s exp\left(-\frac{B}{ln^2 S_s}\right) \quad (17)$$

where A is the kinetic parameter, S_s is the supersaturation index of the reaction products, and B is the thermodynamic parameter. The calculations for these parameters can be found in [18].

Following the nucleation step, thermodynamic modeling is employed to model the chemical reactions and calculate the amount and type of the reaction products that will precipitate. To enhance computational efficiency, the thermodynamic modeling module is invoked for a lattice node without reaction products only when there is a probability of nucleation for at least one primary reaction product (e.g. N-(C-)A-S-H gel) and at least one of secondary reaction products (e.g. zeolites) according to Eq. (16. For lattice cells containing existing reaction products, the thermodynamic modeling module is called directly, bypassing the nucleation probability module. Thermodynamic modeling is performed via GEMS program [32]. The thermodynamic database used in the extended GeoMicro3D model incorporated CEMDATA18 database [33], the thermodynamic data for N-(C-)A-S-H gel [6], C-(N-)A-S-H gel [34], and secondary reaction products [6] of AAFA. Since the N-(C-)A-S-H gel and C-(N-)A-S-H gel in the thermodynamic database only consider chemically bound water, the model additionally incorporates physically bound water for both gel types: (a) For C-(N-)A-S-H gel, the physically bound water includes absorbed water (0.3 mol water per mole of C-(N-)A-S-H gel) and gel pore water ($H_2O/SiO_2 = 4$); (b) For N-(C-)A-S-H gel, the amount of physically bound water is obtained based on its mass loss between 40 and 105 °C in TGA results in [6]. Following the calculation, the compositions of solid phases and pore solution within the lattice cell were updated. The simulation then returned to the dissolution module iteratively until the simulation target time was achieved.

3.2. Simulation of dissolution of fly ash

To evaluate the accuracy of the established dissolution rate function derived from fly ash dissolution measurement (shown in Section 4.2), the dissolution of fly ash in a 5 M sodium hydroxide solution was simulated at 20 °C and 40 °C using the extended GeoMicro3D model. The initial structure consisted of fly ash particles with a maximum size of 10 μm, arranged within a cube of 125 μm × 125 μm × 125 μm. The solution to fly ash mass ratio was 1000, mirroring the conditions of the dissolution experiment. In the simulation, fly ash contains three parts: amorphous particles, crystalline particles and voids. The amorphous and crystalline phases are modeled as separate particles in the model, while particles containing both phases are not explicitly represented. Although only a small fraction of fly ash particles may contain a mixture of amorphous and crystalline phases [10,35], this simplification may slightly affect the microstructural homogeneity, but it is not expected to have a significant impact on the overall simulation results. The fraction of the voids can be determined via the relationship between the apparent volume of fly ash (V_a) and the volume of hollow voids (V_v) in fly ash using the following equation:

$$V_a\rho_a = (V_a - V_v)\rho_r \quad (18)$$

where ρ_a (g/cm^3) and ρ_r (g/cm^3) are the apparent density and the real density of fly ash, respectively. In this work, they are determined as 2.13 g/cm^3 and 2.65 g/cm^3, respectively.

The digitized simulation cube was initialized in terms of element compositions for liquid voxels and fly ash voxels. The model considered oxides including SiO_2, Al_2O_3, CaO, Fe_2O_3, MgO, K_2O and Na_2O for fly ash representation. The amounts of chemical compositions in the amorphous fly ash were aligned with the chemical composition determined in Table 1. Only amorphous fly ash was considered reactive, having the capacity to dissolve, while crystalline fly ash was considered not dissolvable.

The solubility products of SiO_2, Al_2O_3 and CaO, used in Eq. (1), were set as 1.23×10^2, 3.55 and 2.1×10^{-1}, respectively [36]. The parameter f_X in Eq. (7) was set as 0.8, 1.2 and 1.2 for Mg, K and Na, respectively [36]. The parameter f_{Fe} in Eq. (8) was set as 0.2. The diffusivities of various ions used in Eq. (13) are listed in Table 3.

Table 3
Diffusivities of aqueous ions in solution at 25 °C [18].

Ions	SiO_3^{2-}	AlO_2^-	Ca^{2+}	Mg^{2+}	FeO_2^-	K^+	Na^+	OH^-
D_p($\times 10^{-9}$ m^2/s)	0.7	0.6	0.72	0.71	0.6	1.96	1.33	5.28

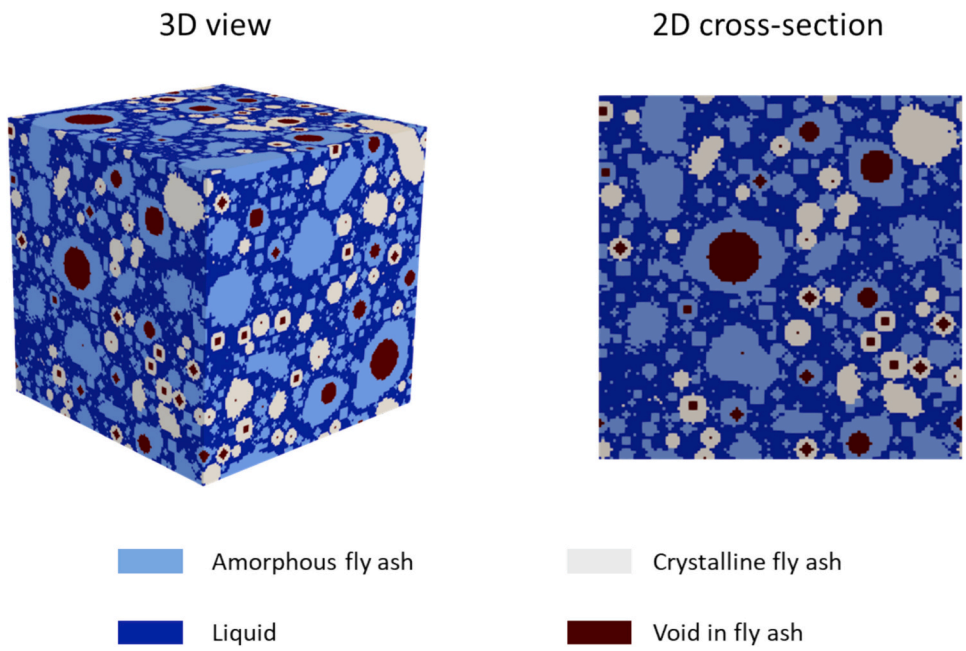

Fig. 4. Initial structure of AAFA with a size of 125 μm × 125 μm × 125 μm and a digitization resolution of 1 μm × 1 μm × 1 μm per voxel.

Table 4
Simulation input and parameters.

Input	Mixture	See Section 2.3
	Temperature	40 °C
	Simulation size	125 μm × 125 μm × 125 μm
Dissolution module	Dissolution rate of fly ash	Eqs. (1), (7)–(9), (20), (21)
	Relative dissolution rate f_X for Mg in Eq. (7)	0.8
	Relative dissolution rate f_X for K in Eq. (7)	1.2
	Relative dissolution rate f_X for Na in Eq. (7)	1.2
	Relative dissolution rate f_{Fe} in Eq. (8)	0.2
	K_{sp} of SiO_2 (in Eq. (1))	1.23×10^2
	K_{sp} of CaO (in Eq. (1))	3.55
	K_{sp} of Al_2O_3 (in Eq. (1))	2.1×10^{-1}
Transportation module	Diffusivity of aqueous ions in solution (D_p)	Table 3
	Diffusivities of aqueous ions in gels	$0.0025 \times D_p$
Nucleation and growth module	Parameters A and B (in Eq. (17))	Same in [18]
Thermodynamic modeling module	Thermodynamic database of reaction products	N-(C-)A-S-H gel [6,7], zeolites [39], Cemdata18 [33][a]
Others	Physically adsorbed water in C-(N-)A-S-H gel	Same in [18]
	Physically adsorbed water in N-(C-)A-S-H gel	11–15 wt% of N-(C-)A-S-H gel[b]

[a] : The thermodynamic database is available in the cited references.
[b] : The total fraction of physically adsorbed water in N-(C-)A-S-H gel in this work was determined based on the mass loss between 40 and 105 °C in TGA results in [6].

3.3. Simulation of the three-dimensional microstructure of AAFA paste

According to its mixture presented in Section 2.3, the initial structure was generated in a cube of 125 μm × 125 μm × 125 μm, as shown in Fig. 4. The resolution was set at 1 μm × 1 μm × 1 μm per voxel. More specifically, the simulation box contains 125 × 125 × 125 voxels, with each voxel occupied by fly ash or alkaline solution. As recommended in [37], the size of the simulation box should be at least 2.5 times larger than the largest particle. Hence, the minimum and maximum particle size of fly ash was set at 1 μm and 50 μm, respectively. Although the simulated particle size is different from the experiment, such difference has been already considered in the model through Eq. (8). The model parameters outlined in Section 3.2 for the dissolution module were also adopted here (shown in Table 4). In addition, C-(N-)A-S-H gel and N-(C-)A-S-H gel were considered as diffusive phases for ions, while the other reaction products were treated as non-diffusive for ions. The relative ion diffusivities through the C-(N-)A-S-H and N-(C-)A-S-H gels were set to 0.0025 times their values in the solution (see Table 3) [38]. Fly ash particles and crystalline reaction products were considered non-diffusive phases. A detailed description of diffusivity of ions through lattice nodes containing both diffusive and non-diffusive phases can be found in [38]. The simulation input and parameters used in the extended GeoMicro3D model to simulate the reaction and microstructure of AAFA are summarized in Table 4.

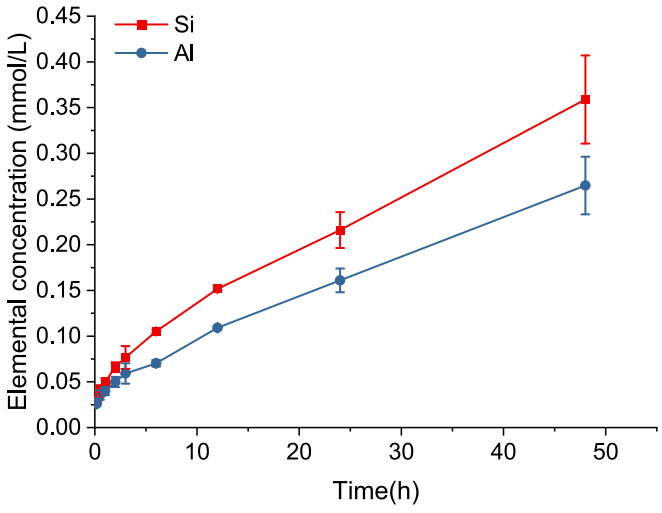

Fig. 5. Measured concentrations of Si and Al for the dissolution of fly ash in a 1.5 M NaOH solution at 20 °C.

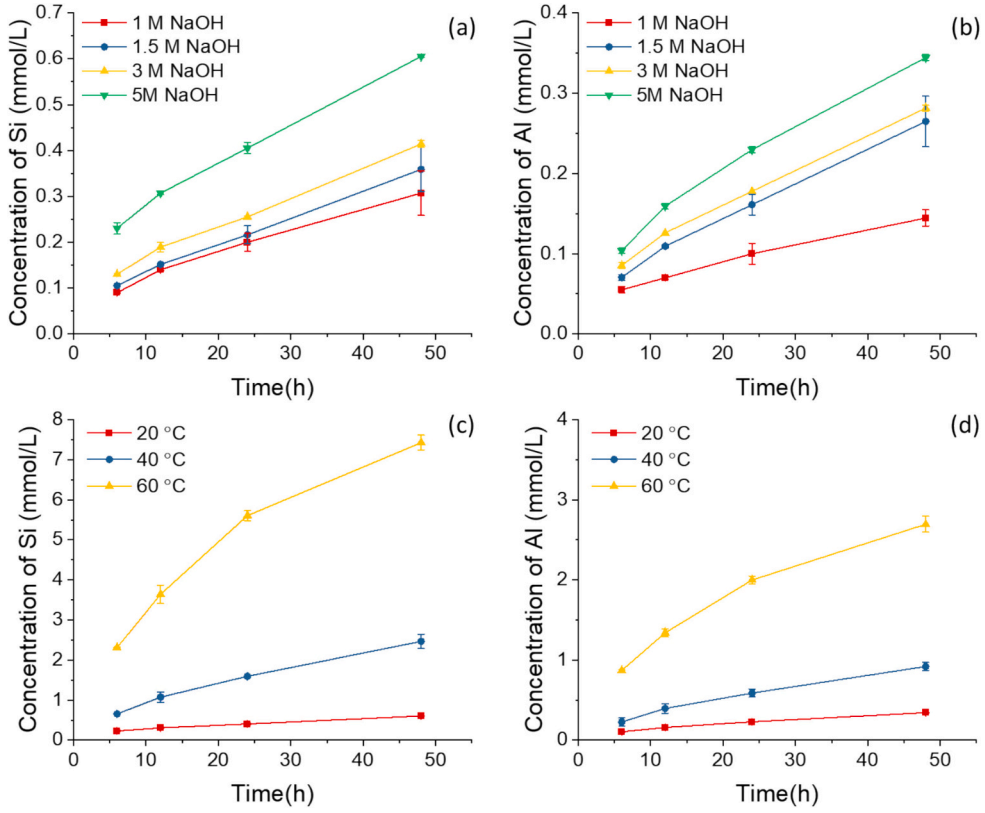

Fig. 6. Measured concentrations of (a) Si and (b) Al for the dissolution of fly ash under different pH conditions at 20 °C; Measured concentrations of (c) Si and (d) Al for the dissolution of fly ash at different temperatures.

4. Results and discussions

4.1. Experimental dissolution of fly ash under different conditions

To gain a basic understanding of the dissolution behavior of fly ash in an alkaline solution, the concentrations of Si and Al were measured from the early stages (5 min) to long-term stages (48 h). The concentration of Si and Al in the solution in a 1.5 M NaOH solution at 20 °C is illustrated in Fig. 5. The data clearly show a non-linear increase in Si and Al concentrations within the initial 6 h, followed by a subsequent linear rise from 6 to 48 h. The dissolution behavior of silicate glass under a far-from-equilibrium condition commonly involves two stages: the non-steady state and the steady state [9,14,17]. In this work, the non-linear stage from 0 to 6 h is referred to as the non-steady state, indicating a varying dissolution rate, while the subsequent linear stage is considered the steady state, indicating a constant dissolution rate. To investigate forward dissolution rate r_+ in the steady state, the elemental concentrations were specifically examined from 6 to 48 h under various pH and temperatures, as detailed below.

The effects of the solution pH and the temperature on the dissolution of fly ash are shown in Fig. 6. At 20 °C, the concentrations of Si and Al exhibited a linear correlation with time from 6 to 48 h, albeit with a slight deviation from linearity observed at the 6-h mark (see Fig. 6(a) and Fig. 6(b)). This observation suggests that the transition from a non-steady state to a steady state occurs within the 6 to 12-h range, irrespective of the solution's alkalinity. A similar observation was found in the dissolution at 40 °C. However, at 60 °C the dissolution rate for both Si and Al did not remain constant but declined after 24 h, as shown in Fig. 6(c) and Fig. 6(d), indicating the end of the steady state. The decrease in the dissolution rate suggests that the dissolution had shifted away from a far-from-equilibrium state. This change is due to the dramatic increase in ion concentration, and thus the ion activity product, over time at 60 °C. As a result, after 24 h of dissolution at 60 °C, the ion activity product became large enough to negatively impact the dissolution rate according to Eq. (1, leading to a decrease in the dissolution rate. Overall, a steady state is consistently observed during dissolution, regardless of the solution pH and the temperature.

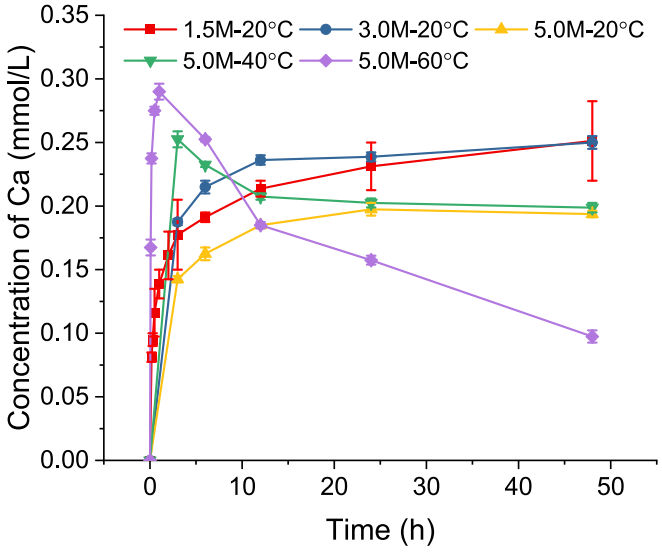

Fig. 7. Measured concentrations of Ca for the dissolution of fly ash under different conditions.

The concentration of Ca over time for the dissolution of fly ash under different conditions (as outlined in Table 2) is shown in Fig. 7. At 20 °C, Ca concentration increased rapidly within 3 h and reached a plateau after 12 h, regardless of the NaOH solution concentration. In contrast, at higher temperatures (40 °C or 60 °C), the initial increase in Ca

concentration was followed by a decrease, indicating the precipitation of Ca-containing reaction products. Both the stabilization at 20 °C and the decrease at higher temperatures mean that the dissolution process has transitioned out of a far-from-equilibrium state. In other words, the dissolution of Ca experiences a very short far-from-equilibrium state before it reaches equilibrium or oversaturation state. During the far-from-equilibrium state, it is also very difficult to distinguish between the non-steady state and the steady state as observed for the dissolution of Si and Al. Thus, the forward dissolution rate of Ca is calculated based on the change in concentration during the initial 0–3 h.

4.2. Forward dissolution rate of fly ash

According to the evolution of elemental concentrations in the steady state measured above, the forward dissolution rate of Si ($r_{+,Si}$) at different pH and temperatures can be calculated using Eq. (3).

To fit η, E_a and k_0 in Eq. (2), the equation was rearranged to a linear relationship as follows:

$$log\, r_+ = \eta^* pH - E_a \frac{\log e}{R^* T} + log\, k_0 \tag{19}$$

Fig. 8 shows the fitting results for the parameters (η, E_a and k_0) in Eq. (19). The relationship between pH of the solution and $log\, r_{+,Si}$ was plotted and fitted in Fig. 8(a). The log forward dissolution rate of Si has a linear relationship with the pH values, with a fitting slope (η) of 0.4. For a constant pH of 14.7, the correlation between the log dissolution rate of Si and temperature was fitted in Fig. 8(b). According to the fitting results ($E_a \frac{\log e}{R}$=3157), the apparent activation energy E_a in Eq. (19) was determined as 60.41 kJ/mol, which is in good agreement with the data obtained in [16]. The parameter k_0 is supposed to be linked to intrinsic properties of silicate glasses. With the determined $log\, r_{+,Si}$, η and E_a, $log\, k_0$ can be calculated using Eq. (19). An index, Ca/(Si + Al) molar ratio, is proposed to represent glass reactivity. Since Ca acts as a network modifier, while Si and Al usually function as network formers, a higher Ca/(Si + Al) refers to a higher reactivity of an aluminosilicate glass. The correlation between $log\, k_0$ and Ca/(Si + Al) of glasses, including fly ash in this study and glasses from [9,36,40], are plotted in Fig. 8(c). The dissolution conditions and forward dissolution rate of the glasses from [9,36,40] are provided in Table A.1 in Appendix. A linear increase in $log\, k_0$ is observed with increasing Ca/(Si + Al), indicating more rapid dissolution in fly ash with higher reactivity.

According to the fitting results shown in Fig. 8, the general function describing the forward dissolution rate of Si (mol/m^2/s) can be expressed as follows:

$$log\, r_{+,Si} = 0.4^* pH - \frac{3157}{T} + 2.83^* \frac{Ca}{Si + Al} - 3.91 \tag{20}$$

Based on the theory of stoichiometric dissolution [9,13], Al and Si in aluminosilicate materials dissolve stoichiometrically. Therefore, the forward dissolution rate of Al is calculated by using Eq. (21).

$$log\, r_{+,Al} = log\left(\frac{\nu_{Al}}{\nu_{Si}} r_{+,Si}\right) = log\left(\frac{\nu_{Al}}{\nu_{Si}}\right) + log r_{+,Si} \tag{21}$$

The forward dissolution rate of Ca is described using the original function developed in GeoMicro3D model:

$$r_{+,Ca} = \left(8.81^* \frac{V_{model}/S_{model}}{V_{exp}/S_{exp}} + 7.26\right)^* 10^{0.1868pH - 8.7729} \tag{22}$$

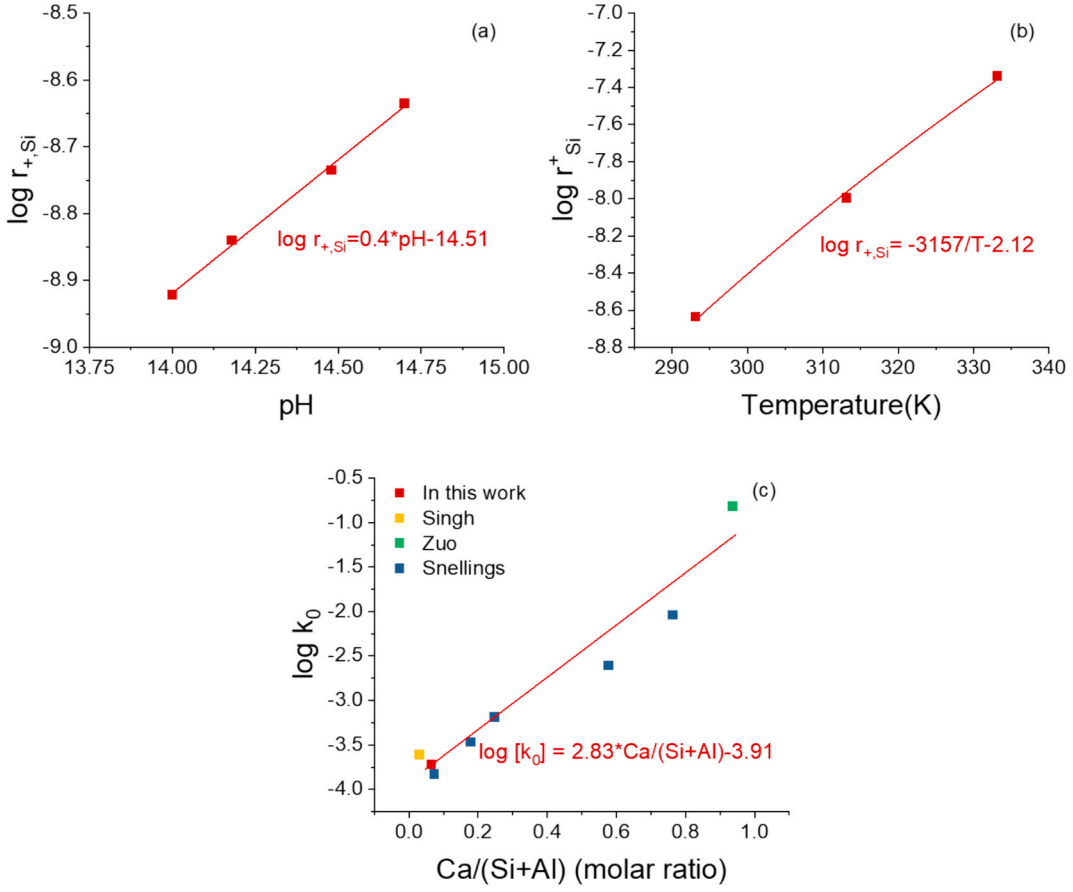

Fig. 8. Forward dissolution rate of Si as a function of (a) pH and (b) temperature; (c) relationship between log k_0 and Ca/(Si + Al) molar ratio in glass. Part of data is obtained from Singh [40], Zuo [36] and Snellings [9].

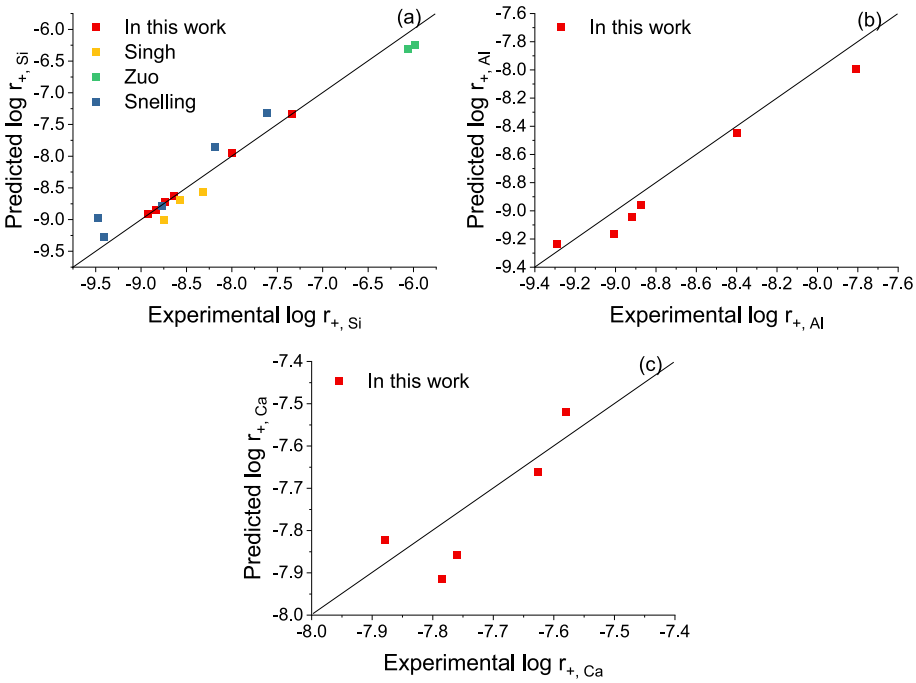

Fig. 9. The correlation between predicted and experimental log forward dissolution rates of (a) Si, (b) Al and (c) Ca. Part of data is obtained from Singh [40], Zuo [36] and Snellings [9]. Note that the log forward dissolution rate from [9] has been recalculated according to Eq. (3).

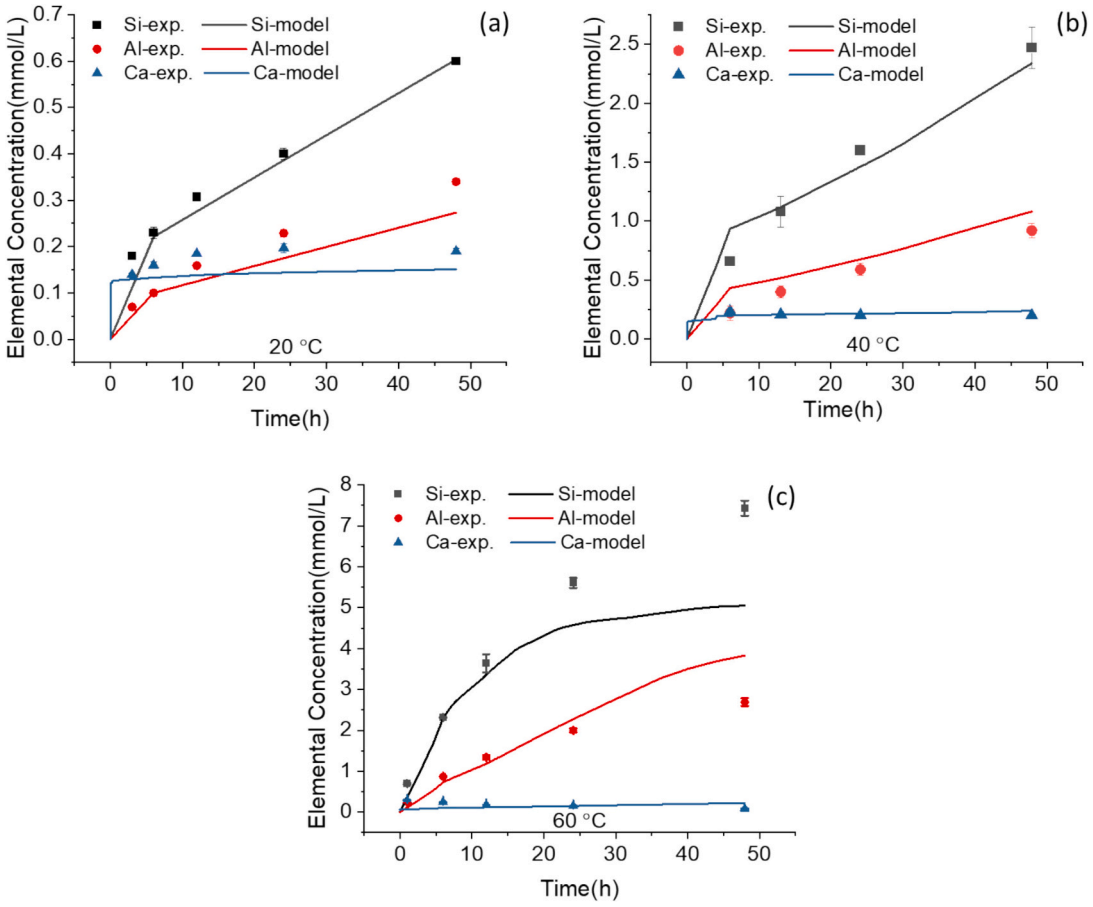

Fig. 10. Comparison of elemental concentrations in fly ash dissolution: simulated and experimental results in a 5 M NaOH solution at (a) 20 °C, (b) 40 °C and (c) 60 °C.

where V_{model} and V_{exp} denote the solution volume in simulation and experiment, respectively, while S_{model} and S_{exp} represent the surface area of the fly ash in simulation and experiment, respectively. The derivation of this equation can be found in [36].

The effect of temperature on the dissolution rate of Ca is considered based on the Arrhenius equation [36]:

$$r_{new} = r_{ref}\exp\left[\frac{E_a}{R}\left(\frac{1}{T_{ref}}-\frac{1}{T_{new}}\right)\right] \quad (23)$$

where r_{new} and r_{ref} are the dissolution rates at the Kelvin temperatures T_{new} and T_{ref}(293.15 K), respectively. E_a is the activation energy of the dissolving element (1.36 × 104 J/mol for CaO). R is the gas constant.

To evaluate the accuracy of these prediction functions, Fig. 9 illustrates the correlation between the predicted and experimental log forward dissolution rates of Si, Al and Ca. Notably, in Fig. 9(a), Eq. (20) demonstrates a precise prediction of the forward dissolution rate of Si for the fly ash investigated in this work. Moreover, its applicability extends to well predicting the forward dissolution rate of Si for other aluminosilicate glasses documented in the literature [9,36,40]. However, due to the limited availability of fly ash dissolution data, the aluminosilicate glass data used for validation in Fig. 9(a) are the same as those used to establish the prediction function (Fig. 8(c)). In future work, incorporating a broader range of fly ashes with diverse chemical compositions and amorphous structures would not only enhance the validation but also contribute to refining the predictive equation itself, thereby improving its robustness and general applicability.

The consistency between the predicted and experimental log forward dissolution rates of Al, as shown in Fig. 9(b), affirms the rationality of predicting the dissolution rate of Al based on that of Si. Fig. 9(c) shows that the forward dissolution rate function for Ca in slag can accurately predict the dissolution rate of Ca in fly ash, with an error margin of less than ±log 0.2. Overall, the strong agreement between predictions and experimental results in Fig. 9 confirms the validity of these dissolution rate functions. Consequently, the newly developed function for predicting the forward dissolution rates of Si will be seamlessly integrated into the GeoMicro3D model for its applicability in AAFA, while original functions of forward dissolution rate of Al and Ca remain unchanged. Besides, to simplify the non-steady-state of fly ash dissolution during the initial 0–6 h period, a constant rate was assumed in the extended GeoMicro3D model. Specifically, this rate was set to be three times the steady-state dissolution rate, based on experimental data shown in Fig. 6. This linear approximation captures the cumulative amount of dissolved Si and Al at 6 h, while underestimating the actual dissolution rate at earlier time points. Despite this simplification, the approach provides a practical representation of early-stage dissolution. Future research should focus on examining the dissolution rate in non-steady state conditions and developing corresponding functions to better represent it.

4.3. Simulated dissolution of fly ash

The dissolution of fly ash in a 5 M NaOH solution was simulated at different temperatures using the GeoMicro3D model modified with the developed dissolution rate functions. Fig. 10 shows the simulated and measured concentrations of Si, Al, and Ca released from the fly ash. The simulated Si concentrations generally match the experimental results, except at 60 °C after 24 h, where modeling concentrations are lower than the experimental ones. This discrepancy may be attributed to the slight dissolution of crystalline fly ash at high temperatures, which was considered completely inert in the simulation. Moreover, at 60 °C, a decrease in the dissolution rate of Si is observed after 24 h in the modeling result, aligning with the experimental findings. In addition, the simulations capture well the evolution of Al and Ca concentrations, showing a good agreement with experimental data. The minor difference between the modeling and experimental Al concentrations can be attributed to slight discrepancies in the predicted and experimentally obtained dissolution rates of Al, as shown in Fig. 9(b). Overall, the agreement between simulation and experimentally obtained results underscores the accuracy of the dissolution rate functions, affirming their capability to faithfully simulate the dissolution of fly ash in an alkaline solution.

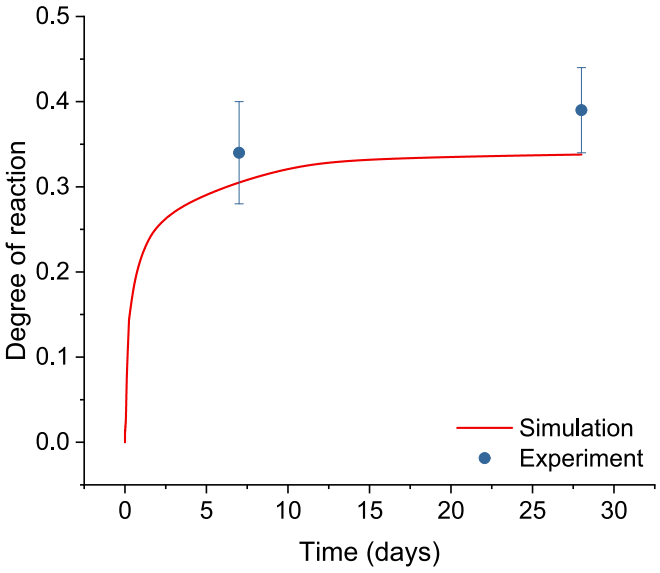

Fig. 11. Simulated degree of reaction of fly ash at 40 °C. Experimental data for the same mixture were obtained from [6].

4.4. Simulation results of AAFA paste

4.4.1. Degree of reaction

The simulated degree of reaction of fly ash as a function of time is shown in Fig. 11, alongside the experimental data for the same mixture at 7 and 28 days obtained in our previous work [6], which measured the reaction degree via image analysis. Note that the definition of degree of fly ash, both in the simulation and experiment, is the ratio of the volume

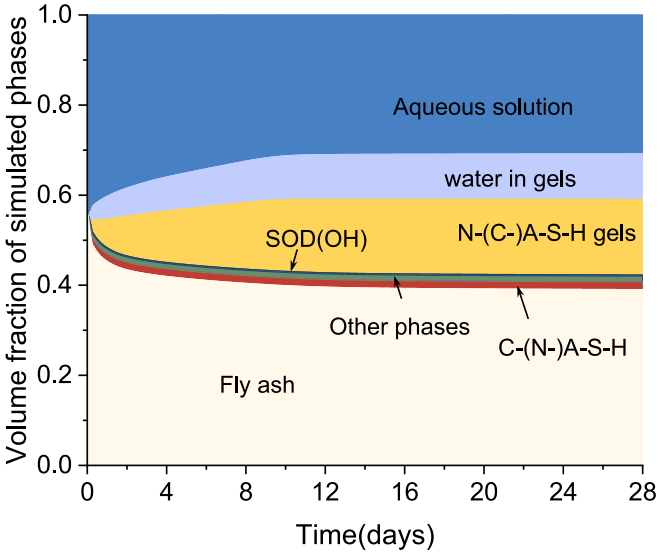

Fig. 12. Phase evolution of simulated phases in AAFA at 40 °C. The label 'Other phases' refers to MgAl-OH-LDH (LDH denotes layered double hydroxide), M-S-H (magnesium silicates hydrate), Brucite ($Mg(OH)_2$), Portlandite ($Ca(OH)_2$) and Ferrihydrite-mc (FeOOH). The label 'water in gels' refers to the physically adsorbed water in C-(N-)A-S-H gel and N-(C-)A-S-H gel.

of reacted fly ash to the initial volume of fly ash (including both amorphous and crystalline fly ash). The degree of reaction of fly ash increased significantly within the first day, followed by a gradual rise subsequently. This trend indicates an initial rapid dissolution of fly ash, which slowed down over time. Initially, fly ash dissolved quickly in the high-pH alkaline solution. However, the dissolution rate of fly ash decreased significantly over time due to two main reasons. First, the pH of the pore solution decreased over time as a result of the reaction between the activator and fly ash, as further confirmed in Fig. 15. Second, the growth of reaction products on the surface of fly ash hindered further interaction between the activator and fly ash, thereby slowing down the dissolution process. This effect is accounted for in the model through Eq. 10. The simulated degree of reaction reached 31 % and 34 % at 7 and 28 days, respectively, slightly lower than the experimental data. The consistency between the simulated and experimental degree of reaction implies that the simulation framework can effectively model the chemical reactions in AAFA.

4.4.2. Phase assemblage

The evolution of simulated phases in AAFA is presented in Fig. 12. The main simulated reaction product of AAFA was N-(C-)A-S-H gel, which is consistent with both the experimental findings in our previous work [6] and other existing literature [41,42]. Minor amounts of C-(N-)A-S-H gel and hydroxysodalite (SOD(OH)) were observed, in accordance with the thermodynamic modeling results for the same mixture in [6]. Besides, a trace amount of portlandite, hydrotalcite (MgAl-OH-LDH), magnesium silicates hydrate (M-S-H), Brucite ($Mg(OH)_2$) and Ferrihydrite-mc (FeOOH) were also formed, collectively presented as the 'other phases' in Fig. 12. These reaction products align with the thermodynamic modeling results for the same mixture in [6], except for portlandite and MgAl-OH-LDH. The variance in reaction products obtained by thermodynamic modeling and GeoMicro3D model can be attributed to the differences in reaction kinetics. More specifically, thermodynamic modeling was based on the congruent dissolution of various oxides in fly ash, whereas GeoMicro3D assigned a specific function of dissolution rate for each oxide. As a result, the chemistry in the pore solution may differ in these two cases, leading to the formation of distinct reaction products. Besides, the physically adsorbed water of C-(N-)A-S-H gel and N-(C-)A-S-H gel was considered in GeoMicro3D, which is another difference compared to the thermodynamic modeling results.

4.4.3. Simulated 3D microstructure

The simulated 3D microstructures of AAFA at 10 mins, 3 h, 7 days and 28 days are shown in Fig. 13. The area in light blue and dark blue represents amorphous fly ash and alkaline activator, respectively. Upon contact with the alkaline activator, the amorphous fly ash particles underwent dissolution, forming a distinct reaction front zone (depicted in orange color). In contrast, the crystalline fly ash particles, represented by light grey, remained unreactive and undissolved, with no development of a reaction front zone around them. At 3 h, a layer of reaction products, shown in red, began to form around the amorphous fly ash particles, with a few reaction products also forming on the surface of the crystalline fly ash particles due to ion transport. As the reaction proceeded, more reaction products emerged, connecting the fly ash particles to construct a solid microstructure. By 7 days, most liquid nodes were filled with reaction products as shown in Fig. 13(c). The microstructure at 28 days, as shown in Fig. 13(d), appeared similar to that at 7

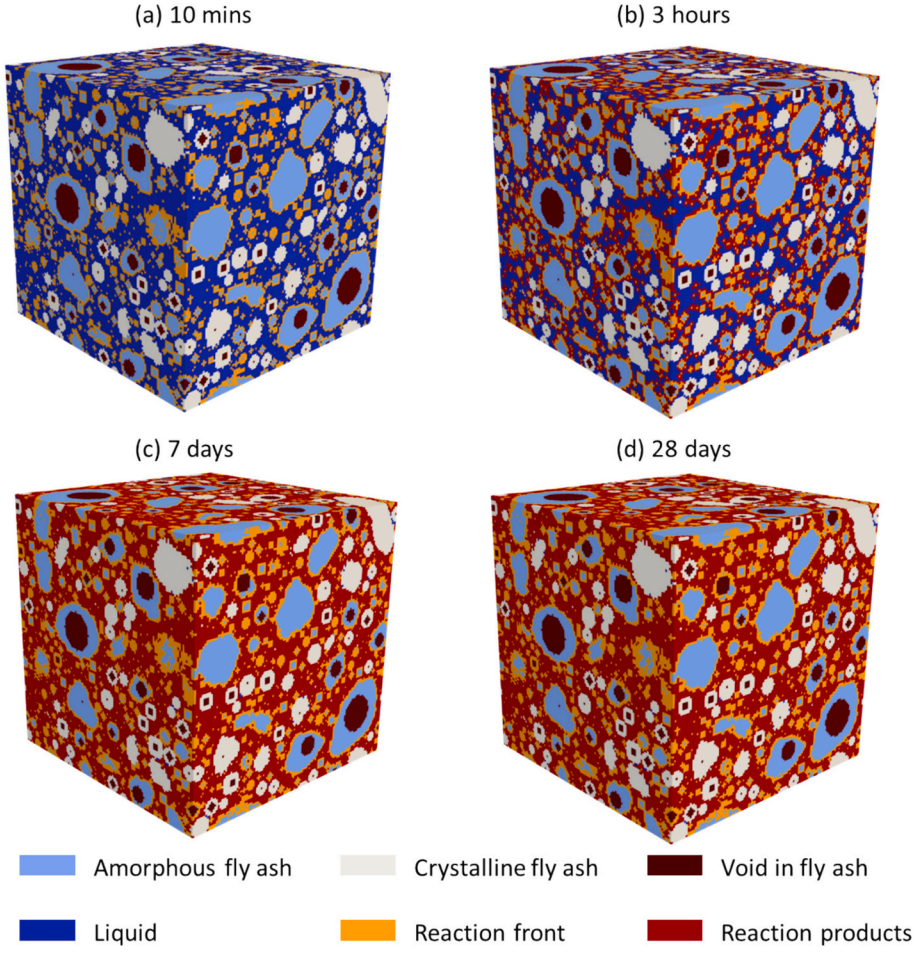

Fig. 13. Simulated 3D microstructure of AAFA at (a) 10mins, (b) 3 h, (c) 7 days and (d) 28 days.

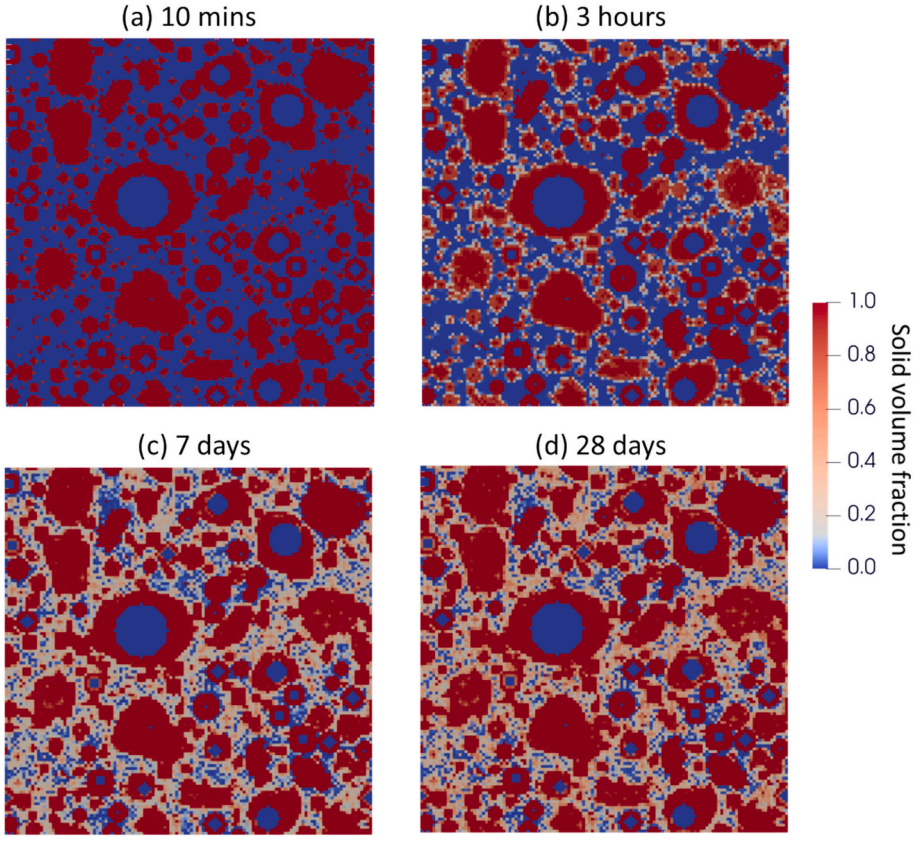

Fig. 14. Solid volume fraction of voxels of cross sections of AAFA at (a) 10 mins, (b) 3 h, (c) 7 days and (d) 28 days. The color scale represents the local solid fraction, ranging from blue (0 %, liquid phase) to dark red (100 % solid content), with light red to dark red indicating increasing solid volume fraction. (For interpretation of the references to color in this figure legend, the reader is referred to the web version of this article.)

Table 5
Comparison of the porosity of AAFA obtained from simulation and experiment.

Porosity	GeoMicro3D	Experiment
7 days	38 %	37 %
28 days	35 %	34 %

days. One reason is that the reaction became very slow from 7 days to 28 days, as can be seen from Fig. 11. Notably, in Fig. 11, any voxel containing partially or completely filled reaction products is marked in red, as results the apparent differences in changes in the amount of reaction products can't be observed from 7 to 28 days. For a more detailed understanding of the evolution of simulated microstructure, it is worthwhile to view the solid volume fraction of each voxel in the simulated box, as further shown below.

Fig. 14 shows the simulated solid volume fraction of voxels in cross-sections of AAFA microstructure at 10 mins, 3 h, 7 days and 28 days. In the beginning, each voxel was either occupied by fly ash (100 % solid) or liquid (0 % solid). As the reaction progressed, the solid volume fraction in the voxels of the amorphous fly ash particle in contact with the alkaline solution decreased, indicating a dissolving fly ash. In contrast, an increase in the solid volume fraction is observed in the voxels that were originally liquid, indicating the formation of reaction products. Over time, a more compact microstructure develops. Additionally, a higher fraction of reaction products accumulated around the amorphous fly ash particles, while a relatively porous structure developed within the spaces between the fly ash particles. This is in accordance with the observation from SEM images for the same mixture in [6].

4.4.4. Porosity of AAFA

Table 5 compares the porosity of AAFA obtained from simulation and experiment, i.e. MIP. The porosity obtained by using MIP at 7 days and 28 days was 37 % and 34 %, respectively. These results were in good agreement with the porosity of the sample 'FA_N9.3S0T40' in [38], which employed an identical mixture. In the simulation, the porosity of the simulated structure was defined as the sum of the volume fraction of the aqueous phase (see Fig. 12) and the hollow voids in fly ash. As shown in Table 5, there is a good agreement between the simulated porosity and experimental results.

4.4.5. Pore solution chemistry

The evolution of simulated elemental concentrations in the pore solution is shown in Fig. 15, alongside the experimental data for the same mixture at 7 and 28 days in our previous work [6]. The concentration of Si initially increased over time, followed by a decrease after 2 days. This trend matches well with experimental observations. During the early simulation period, the reaction was dominated by the dissolution of fly ash, while the formation of reaction products prevailed once a sufficient quantity of ions dissolved in the pore solution. The competition between the dissolution and the formation of reaction products leads to the initial increase and subsequent decrease in the concentration of Si in the pore solution. However, the simulated Si concentration was underestimated compared to experimental data, especially at 28 days. This discrepancy may stem from the underestimated reaction degree. As shown in Fig. 11, the underestimation of the simulated reaction degree at 28 days is more pronounced than at 7 days, leading to a greater discrepancy between the simulated Si concentration and the experimental data at 28 days compared to 7 days. Additionally, the GeoMicro3D model assumes that voids created by chemical shrinkage are automatically filled with water, which could further contribute to the

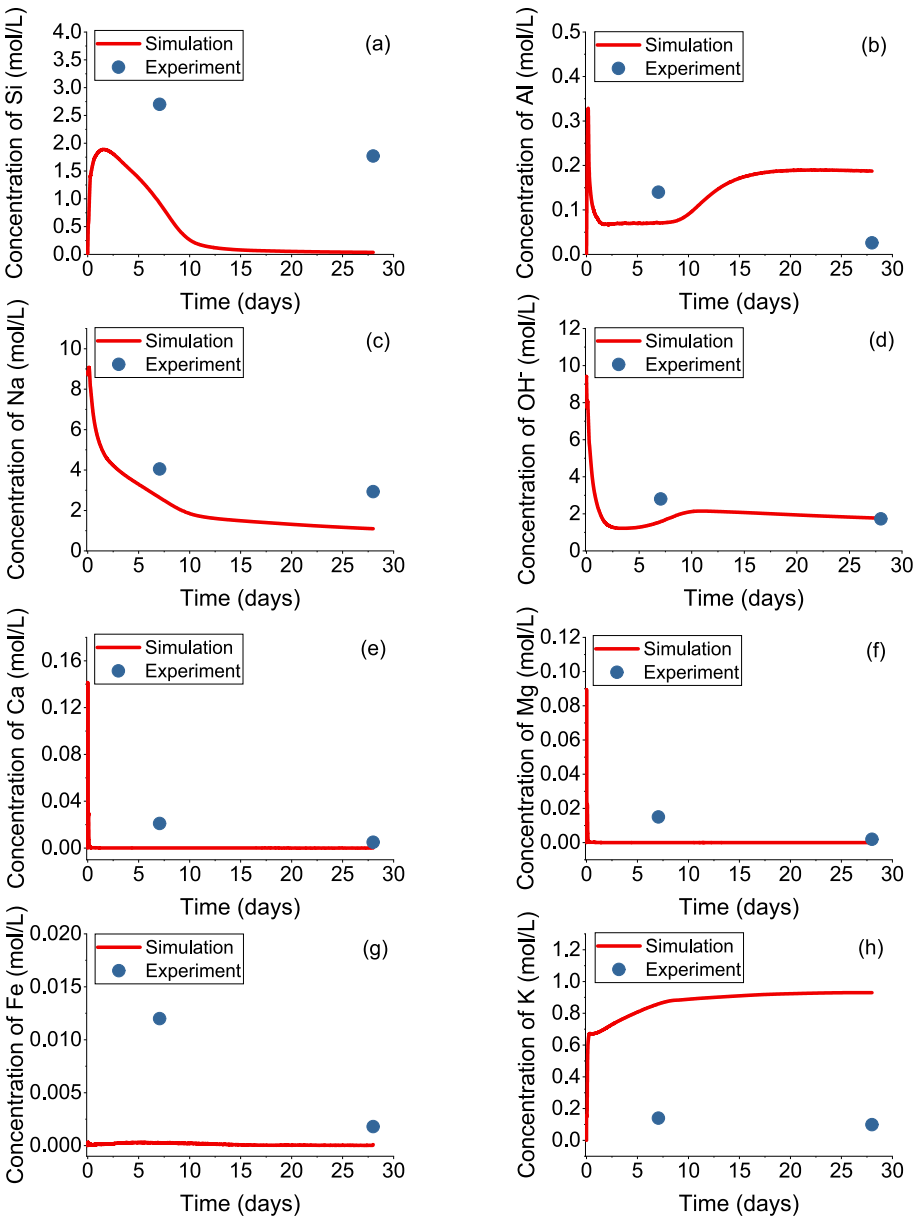

Fig. 15. Simulated element concentrations in comparison with the experimental data for the same mixture in [6].

underestimation of Si concentration in the pore solution.

Similarly, the concentration of Al initially paralleled the trend observed for Si but dropped much earlier, which occurred after a few hours, coinciding with the formation of N-(C-)A-S-H gel as can be seen in Fig. 12. The simulated concentration of Al at 7 days is close to the experimental data. However, after 9 days, the concentration of Al increased slightly again while the concentration of Si started to decline. As a result, the simulated concentration of Al at 28 days is higher than the experimental result. It can be seen from Fig. 15(a) that there were no sufficient Si ions in the pore solution. This limited the formation of reaction products, such as N-(C-)A-S-H gel, leading to the slight increase of Al concentration due to the slow yet ongoing dissolution of fly ash.

Apart from a slight initial increase due to the dissolution of fly ash, the Na concentration mainly decreased over time, resulting from the formation of C-(N-)A-S-H gel, SOD(OH) and N-(C-)A-S-H gel. The concentration of OH^- experienced a dramatic decrease and remained relatively stable after 2 days. The drop in the concentration of OH^- can be attributed to the consumption of OH^- during the dissolution of fly ash. Both simulated concentrations of Na and OH^- were close to the experimental results at 7 days and 28 days.

Both simulated Ca and Mg concentrations rose sharply in the beginning due to their rapid dissolution rates, followed by a sudden drop due to the rapid formation of Ca- and Mg-containing phases. After that, their concentrations remained at very low levels, showing slightly underestimation compared to experimental results. This is because the pore solution in reality is usually oversaturated [43], while the model calculation is based on an equilibrium condition. Additionally, crystalline phases that form in reality may have a poor crystalline structure with higher solubility, whereas these phases in the modeling are considered well-crystallized. This can also contribute to a higher concentration observed experimentally. Similar underestimation is noted for Fe concentration for the same reasons. However, unlike Ca or Mg, Fe did not show a significant initial increase, as its dissolution rate is much slower than that of the other two elements.

The simulated K concentration showed a continuous increase and was higher than the experimental data. This is related to the absence of a solid K-containing phase in the modeling due to a lack of relevant database, while in reality the dissolved K might be incorporated into N-

A-S-H gel to form (N,*K*)-A-S-H gel. As a result, all dissolved K remains in the aqueous phase during simulation, leading to a sustained increase and overestimation of its concentration.

4.4.6. Model limitations and future perspectives

While the extended GeoMicro3D model demonstrates strong predictive capabilities for simulating the reaction kinetics and 3D microstructure evolution of AAFA material, several limitations remain that need to be addressed in future studies. First of all, due to the limited availability of fly ash dissolution data, the same dataset was used to both develop and validate the predictive dissolution function (Eq. 20). In addition, the extended GeoMicro3D model was applied and validated using only a single type of fly ash. Given the well-known variability in fly ash composition and reactivity, further validation using a broader range of fly ash samples is necessary to confirm the generalizability of the model. Moreover, future studies should include systematic sensitivity analyses to quantify how key input parameters, such as amorphous fly ash content, particle size distribution, and chemical composition, influence the model outputs. This would help identify which parameters most significantly affect reaction degree and microstructure development. Also, the dissolution of fly ash experiences a short period of non-steady state before reaching a steady state. In this study, simplifications were made to address this initial period, but the dissolution kinetics during this phase require further investigation in future work for more accurate modeling of the entire dissolution process. It should also be noted that crystalline fly ash is assumed to be totally inert in the model, while it might dissolve at high temperatures in reality as shown in Fig. 10(c). Last, the model adopts thermodynamic modeling to simulate the chemical reactions, assuming a thermodynamic equilibrium. While in reality, some metastable phases may form, and solid-phase transformations can occur as the pore solution evolves. Incorporating these dynamic processes into the model would enhance its accuracy and predictive capability.

5. Conclusions

This study conducted a dissolution test of fly ash in alkaline solutions to develop a prediction function for its dissolution rate. This established dissolution rate function, along with the previously developed thermodynamic database of N-(C-)A-S-H gel, is incorporated into the GeoMicro3D model for application in alkali-activated fly ash (AAFA) system. The extended GeoMicro3D model is then employed to simulate the reactions and evolving microstructure of AAFA paste, and its reliability was validated through comparison with both chemical data (e.g., elemental dissolution trends) and microstructural metrics (e.g., porosity). Based on the results and discussion, the following key conclusions are drawn:

1. A predictive function for fly ash dissolution rate, accounting for pH, temperature, and fly ash reactivity, was developed. This function accurately predicts the dissolution rates of various aluminosilicate glasses.
2. With the newly developed prediction function, the updated GeoMicro3D model successfully simulated the dissolution behavior of fly ash in alkaline solution at different temperatures. The simulated evolution of Si, Al and Ca concentrations closely match the experimental data.
3. The extended GeoMicro3D model accurately simulates the chemical reactions and 3D microstructure of NaOH-based activated fly ash paste. The simulated degree of reaction and the porosity align well with experimental results. Moreover, the simulated reaction products and pore solution chemistry were in good agreement with experiments, with minor differences analyzed.

For the first time, the distribution of different phases in the 3D microstructure of AAFA can be dynamically modeled as a function of time. As the only available tool for such simulations, this model provides fundamental insights into reaction processes and offers a predictive basis for linking microstructural development to engineering performance. This enables its use in mix design optimization, durability assessment, and broader practical applications of AAFA in sustainable construction. Moreover, the extended GeoMicro3D framework offers a modular and versatile platform that allows integration of customizable kinetics and thermodynamic datasets, making it applicable to a broad range of alkali-activated systems.

Supplementary data to this article can be found online at https://doi.org/10.1016/j.cemconres.2025.107999.

CRediT authorship contribution statement

Yun Chen: Writing – original draft, Methodology, Investigation, Conceptualization. **Jiayi Chen:** Methodology. **Mayank Gupta:** Writing – review & editing, Methodology. **Xuhui Liang:** Investigation. **Luiz Miranda de Lima:** Investigation. **Zhiyuan Xu:** Investigation. **Yibing Zuo:** Methodology. **Suhong Yin:** Supervision. **Qijun Yu:** Supervision. **Guang Ye:** Writing – review & editing, Supervision.

Declaration of competing interest

The authors declare the following financial interests/personal relationships which may be considered as potential competing interests: Yun Chen reports financial support was provided by China Scholarship Council. If there are other authors, they declare that they have no known competing financial interests or personal relationships that could have appeared to influence the work reported in this paper.

Acknowledgments

The first author would like to acknowledge China Scholarship Council (Grant No. 201906150022) for the financial support of Yun Chen.

Data availability

Data will be made available on request.

References

[1] A. Fernández-Jiménez, A. Palomo, New cementitious materials based on alkali-activated fly ash: performance at high temperatures, J. Am. Ceram. Soc. 91 (2008) 3308–3314.
[2] Z. Zhang, J.L. Provis, J. Zou, A. Reid, H. Wang, Toward an indexing approach to evaluate fly ashes for geopolymer manufacture, Cem. Concr. Res. 85 (2016) 163–173, https://doi.org/10.1016/j.cemconres.2016.04.007.
[3] M. Criado, A. Fernández-Jiménez, A. Palomo, Alkali activation of fly ash: effect of the SiO2/Na2O ratio. Part I: FTIR study, Microporous Mesoporous Mater. 106 (2007) 180–191, https://doi.org/10.1016/j.micromeso.2007.02.055.
[4] E.D. Rodríguez, S.A. Bernal, J.L. Provis, J. Paya, J.M. Monzo, M.V. Borrachero, Effect of nanosilica-based activators on the performance of an alkali-activated fly ash binder, Cem. Concr. Compos. 35 (2013) 1–11, https://doi.org/10.1016/j.cemconcomp.2012.08.025.
[5] G. Kovalchuk, A. Fernández-Jiménez, A. Palomo, Alkali-activated fly ash: effect of thermal curing conditions on mechanical and microstructural development - part II, Fuel 86 (2007) 315–322, https://doi.org/10.1016/j.fuel.2006.07.010.
[6] Y. Chen, B. Ma, J. Chen, Z. Li, X. Liang, L. Miranda, D. Lima, C. Liu, S. Yin, Q. Yu, B. Lothenbach, G. Ye, Thermodynamic modeling of alkali-activated fly ash paste, Cem. Concr. Res. 186 (2024) 107699, https://doi.org/10.1016/j.cemconres.2024.107699.
[7] Y. Chen, L.M. de Lima, Z. Li, B. Ma, B. Lothenbach, Synthesis, solubility and thermodynamic properties of N-A-S-H gels with various target Si / Al ratios, Cem. Concr. Res. 180 (2024) 107484, https://doi.org/10.1016/j.cemconres.2024.107484.
[8] T. Oey, A. Kumar, I. Pignatelli, Y. Yu, N. Neithalath, J.W. Bullard, M. Bauchy, G. Sant, Topological controls on the dissolution kinetics of glassy aluminosilicates, J. Am. Ceram. Soc. 100 (2017) 5521–5527, https://doi.org/10.1111/jace.15122.
[9] R. Snellings, Solution-controlled dissolution of supplementary cementitious material glasses at pH 13: the effect of solution composition on glass dissolution rates, J. Am. Ceram. Soc. 96 (2013) 2467–2475, https://doi.org/10.1111/jace.12480.

[10] C. Kuenzel, N. Ranjbar, Dissolution mechanism of fly ash to quantify the reactive aluminosilicates in geopolymerisation, Resour. Conserv. Recycl. 150 (2019) 104421, https://doi.org/10.1016/j.resconrec.2019.104421.
[11] C. Chen, W. Gong, W. Lutze, I.L. Pegg, J. Zhai, Kinetics of fly ash leaching in strongly alkaline solutions, J. Mater. Sci. 46 (2011) 590–597, https://doi.org/10.1007/s10853-010-4997-z.
[12] C. Li, Y. Li, H. Sun, L. Li, The composition of fly ash glass phase and its dissolution properties applying to geopolymeric materials, J. Am. Ceram. Soc. 94 (2011) 1773–1778, https://doi.org/10.1111/j.1551-2916.2010.04337.x.
[13] T.M. Iwalewa, T. Qu, I. Farnan, Investigation of the maximum dissolution rates and temperature dependence of a simulated UK nuclear waste glass in circum-neutral media at 40 and 90°C in a dynamic system, Appl. Geochem. 82 (2017) 177–190, https://doi.org/10.1016/j.apgeochem.2017.05.018.
[14] E.H. Oelkers, General kinetic description of multioxide silicate mineral and glass dissolution, Geochim. Cosmochim. Acta 65 (2001) 3703–3719, https://doi.org/10.1016/S0016-7037(01)00710-4.
[15] P. Aagaard, H.C. Helgeson, Thermodynamic and kinetic constraints on reaction rates among minerals and aqueous solutions: I, theoretical considerations, Am. J. Sci. 282 (1982) 237–285.
[16] J.D. Vienna, J.J. Neeway, J.V. Ryan, S.N. Kerisit, Impacts of glass composition, pH, and temperature on glass forward dissolution rate, Materials Degradation 2 (2018) 1–12, https://doi.org/10.1038/s41529-018-0042-5.
[17] E.M. Pierce, E.A. Rodriguez, L.J. Calligan, W.J. Shaw, B. Pete McGrail, An experimental study of the dissolution rates of simulated aluminoborosilicate waste glasses as a function of pH and temperature under dilute conditions, Appl. Geochem. 23 (2008) 2559–2573, https://doi.org/10.1016/j.apgeochem.2008.05.006.
[18] Y. Zuo, G. Ye, GeoMicro3D: a novel numerical model for simulating the reaction process and microstructure formation of alkali-activated slag, Cem. Concr. Res. 141 (2021), https://doi.org/10.1016/j.cemconres.2020.106328.
[19] N.S. Martys, Diffusion in partially-saturated porous materials, Materials and Structures/Materiaux et Constructions 32 (1999) 555–562, https://doi.org/10.1007/bf02480489.
[20] M. Zhang, G. Ye, K. Van Breugel, Modeling of ionic diffusivity in non-saturated cement-based materials using lattice Boltzmann method, Cem. Concr. Res. 42 (2012) 1524–1533, https://doi.org/10.1016/j.cemconres.2012.08.005.
[21] L. Liu, X. Wang, H. Chen, C. Wan, M. Zhang, Numerical modeling of drying shrinkage deformation of cement-based composites by coupling multiscale structure model with 3D lattice analyses, Comput. Struct. 178 (2017) 88–104, https://doi.org/10.1016/j.compstruc.2016.10.005.
[22] B. Pichler, C. Hellmich, Upscaling quasi-brittle strength of cement paste and mortar: a multi-scale engineering mechanics model, Cem. Concr. Res. 41 (2011) 467–476, https://doi.org/10.1016/j.cemconres.2011.01.010.
[23] T.-S. Han, D. Eum, S.-Y. Kim, J.-S. Kim, J.-H. Lim, K. Park, D. Stephan, Multi-scale analysis framework for predicting tensile strength of cement paste by combining experiments and simulations, Cem. Concr. Compos. 139 (2023) 105006, https://doi.org/10.1016/j.cemconcomp.2023.105006.
[24] ASTM C618-19, Standard Specification for Coal Fly Ash and Raw or Calcined Natural Pozzolan for Use in Concrete, ASTM International, West Conshohocken, 2019.
[25] Z. Qian, E.J. Garboczi, G. Ye, E. Schlangen, Anm: a geometrical model for the composite structure of mortar and concrete using real-shape particles, Mater. Struct. 49 (2016) 149–158, https://doi.org/10.1617/s11527-014-0482-5.
[26] Y. Zuo, Z. Qian, E.J. Garboczi, G. Ye, Numerical simulation of the initial particle parking structure of cement/geopolymer paste and the dissolution of amorphous silica using real-shape particles, Constr. Build. Mater. (2018), https://doi.org/10.1016/j.conbuildmat.2018.07.063.
[27] E.H. Oelkers, General Kinetic Description of Multioxide Silicate Mineral and Glass Dissolution, 2001.
[28] G. Berger, C. Claparols, Christophe Guy, V. Daux, Dissolution rate of a basalt glass in silica-rich solutions: implications for long-term alteration, Geochim. Cosmochim. Acta 58 (1994) 4875–4886.
[29] M. Gupta, X. Qiu, M. Omran, Y. Chen, M. Khalifeh, G. Ye, Reaction and microstructure development of one-part geopolymer for wellbore applications – an experimental and numerical study, Cem. Concr. Res. 188 (2025), https://doi.org/10.1016/j.cemconres.2024.107738.
[30] Q. Kang, S. Chen, Lattice Boltzmann simulation of chemical dissolution in porous media, Phys. Rev. E 65 (2002) 1–8, https://doi.org/10.1103/PhysRevE.65.036318.
[31] S. Jiang, J.H. Ter Horst, Crystal nucleation rates from probability distributions of induction times, Cryst. Growth Des. 11 (2010) 256–261, https://doi.org/10.1021/cg101213q.
[32] D.A. Kulik, T. Wagner, S.V. Dmytrieva, G. Kosakowski, F.F. Hingerl, K. V. Chudnenko, U.R. Berner, GEM-Selektor geochemical modeling package: revised algorithm and GEMS3K numerical kernel for coupled simulation codes, Comput. Geosci. 17 (2013) 1–24, https://doi.org/10.1007/s10596-012-9310-6.
[33] B. Lothenbach, D.A. Kulik, T. Matschei, M. Balonis, L. Baquerizo, B.Z. Dilnesa, G. D. Miron, Cemdata18: a chemical thermodynamic database for hydrated Portland cements and alkali-activated materials, Cem. Concr. Res. (2019) 472–506, https://doi.org/10.1109/ICCPS.2014.6843714.
[34] R.J. Myers, S.A. Bernal, J.L. Provis, A thermodynamic model for C-(N-)A-S-H gel: CNASH-ss. Derivation and validation, Cem. Concr. Res. 66 (2014) 27–47, https://doi.org/10.1016/j.cemconres.2014.07.005.
[35] D.P. Bentz, S. Remond, Incorporation of Fly Ash into a 3-D Cement Hydration Microstructure Model, National Institute of Standards and Technology, 1997.
[36] Y. Zuo, G. Ye, Lattice Boltzmann simulation of the dissolution of slag in alkaline solution using real-shape particles, Cem. Concr. Res. 140 (2021), https://doi.org/10.1016/j.cemconres.2020.106313.
[37] Z. Qian, E. Schlangen, G. Ye, K. van Breugel, Modeling framework for fracture in multiscale cement-based material structures, Materials 10 (2017), https://doi.org/10.3390/ma10060587.
[38] Y. Zuo, Experimental Study and Numerical Simulation of the Reaction Process and Microstructure Formation of Alkali-activated Materials, 2019, https://doi.org/10.4233/uuid.
[39] B. Ma, B. Lothenbach, Synthesis, characterization, and thermodynamic study of selected Na-based zeolites, Cem. Concr. Res. 135 (2020) 106111, https://doi.org/10.1016/j.cemconres.2020.106111.
[40] G.V.P.B. Singh, C. Subrahmanyam, K.V.L. Subramaniam, Dissolution of the glassy phase in low-calcium fly ash during alkaline activation, Adv. Cem. Res. 30 (2018) 313–322, https://doi.org/10.1680/jadcr.17.00170.
[41] A. Fernández-Jiménez, A. Palomo, Composition and microstructure of alkali activated fly ash binder: effect of the activator, Cem. Concr. Res. 35 (2005) 1984–1992, https://doi.org/10.1016/j.cemconres.2005.03.003.
[42] G.V.P. Bhagath Singh, K.V.L. Subramaniam, Influence of processing temperature on the reaction product and strength gain in alkali-activated fly ash, Cem. Concr. Compos. 95 (2019) 10–18, https://doi.org/10.1016/j.cemconcomp.2018.10.010.
[43] W.F. Lothenbach B, Thermodynamic modelling of the hydration of Portland cement, Cem. Concr. Res. 36 (2006) 209–226.